AGU PUBLICATIONS

JGR

Journal of Geophysical Research: Space Physics

RESEARCH ARTICLE

10.1002/2017JA024152

Electron heating and energy inventory during asymmetric reconnection in a laboratory plasma

Jongsoo Yoo[1], Byungkeun Na[2], J. Jara-Almonte[1], Masaaki Yamada[1], Hantao Ji[1], V. Roytershteyn[3], M. R. Argall[4], W. Fox[1], and Li-Jen Chen[5]

[1]Princeton Plasma Physics Laboratory, Princeton, New Jersey, USA, [2]National Fusion Research Institute, Daejeon, South Korea, [3]Space Science Institute, Boulder, Colorado, USA, [4]Space Science Center, University of New Hampshire, Durham, New Hampshire, USA, [5]Department of Astronomy, University of Maryland, College Park, Maryland, USA

Key Points:
- Features of asymmetric reconnection such as bipolar Hall magnetic fields are confirmed in laboratory
- Electron heating near the low-density side separatrices is mainly caused by the parallel electric field
- The energy inventory of MRX asymmetric reconnection shows comparable ion and electron energy gains

Correspondence to:
J. Yoo,
jyoo@pppl.gov

Citation:
Yoo, J., B. Na, J. Jara-Almonte, M. Yamada, H. Ji, V. Roytershteyn, M. R. Argall, W. Fox, and L.-J. Chen (2017), Electron heating and energy inventory during asymmetric reconnection in a laboratory plasma, *J. Geophys. Res. Space Physics*, *122*, 9264–9281, doi:10.1002/2017JA024152.

Received 15 MAR 2017
Accepted 27 JUL 2017
Accepted article online 2 AUG 2017
Published online 11 SEP 2017

Abstract Electron heating and the energy inventory during asymmetric reconnection are studied in the laboratory plasma with a density ratio of about 8 across the current sheet. Features of asymmetric reconnection such as the large density gradients near the low-density side separatrices, asymmetric in-plane electric field, and bipolar out-of-plane magnetic field are observed. Unlike the symmetric case, electrons are also heated near the low-density side separatrices. The measured parallel electric field may explain the observed electron heating. Although large fluctuations driven by lower hybrid drift instabilities are also observed near the low-density side separatrices, laboratory measurements and numerical simulations reported here suggest that they do not play a major role in electron energization. The average electron temperature increase in the exhaust region is proportional to the incoming magnetic energy per an electron/ion pair but exceeds scalings of the previous space observations. This discrepancy is explained by differences in the boundary condition and system size. The profile of electron energy gain from the electric field shows that there is additional electron energy gain associated with the electron diamagnetic current besides a large energy gain near the X line. This additional energy gain increases electron enthalpy, not the electron temperature. Finally, a quantitative analysis of the energy inventory during asymmetric reconnection is conducted. Unlike the symmetric case where the ion energy gain is about twice more than the electron energy gain, electrons and ions obtain a similar amount of energy during asymmetric reconnection.

Plain Language Summary In the Magnetic Reconnection Experiment at Princeton Plasma Physics Laboratory, quantitative studies of magnetic reconnection have been performed over the last two decades. In this study, we present results from asymmetric reconnection, which occurs at the dayside magnetopause. We observed remarkable similarities between space and laboratory data regarding general features of asymmetric reconnection, which verifies earlier space observations. In addition, we carried out quantitative analysis on the electron heating and concluded that the electric field along the magnetic field plays an important role. Finally, the energy inventory, which regards how much of the magnetic energy is converted different forms of energy during reconnection, is carried out in this asymmetric laboratory plasma and shows similarities and differences, compared to the previous symmetric case. This quantitative study of the energy inventory is difficult to achieve via space data due to the limitation of the space measurements such as the number of data points, although it is important since the most important feature of magnetic reconnection is the ability to convert magnetic energy to plasma energy.

1. Introduction

Magnetic reconnection, a topological rearrangement of magnetic field lines, facilitates fast conversion from magnetic to plasma energy. Over the last decade, asymmetric reconnection, where there are significant differences in plasma parameters such as the density, temperature, and magnetic field strength across the current sheet, has been studied extensively due to its generality and applicability to reconnection at the dayside magnetopause [e.g., *Mozer and Pritchett*, 2011; *Eastwood et al.*, 2013a]. Asymmetric reconnection shows different features from symmetric reconnection; in particular, profiles of the Hall fields—the out-of-plane quadrupole magnetic field and in-plane bipolar electric field become almost bipolar and unipolar, respectively [*Pritchett*, 2008; *Tanaka et al.*, 2008; *Mozer et al.*, 2008a; *Malakit et al.*, 2010; *Mozer et al.*, 2008a, 2008b; *Yoo et al.*, 2014a].

Since the Hall fields play important roles in energy conversion during reconnection [*Yoo et al.*, 2013, 2014b; *Yamada et al.*, 2014], detailed energy conversion processes can be different in asymmetric reconnection. Thus, it is timely and important to discuss how and where electrons and ions obtain energy during asymmetric reconnection.

Bulk electron heating during reconnection has drawn relatively less attention from the community, compared to energetic electron generation, which is related to the abundance of X-rays during solar flare [*Lin and Hudson*, 1976; *Lin et al.*, 2003; *Krucker et al.*, 2010]. However, it is usually the bulk electron population that carries most of energy during reconnection, such that understanding bulk electron heating is more important in terms of the energy budget during reconnection. Recently, attempts on understanding how electron heating depends on plasma parameters flowing in the reconnection region have been made [*Phan et al.*, 2013; *Shay et al.*, 2014; *Haggerty et al.*, 2015]. Bulk electron heating is found to be proportional to the incoming magnetic energy per an electron/ion pair [*Phan et al.*, 2013; *Shay et al.*, 2014], but the parallel electric field plays an important role in determining the amount of electron and ion heating [*Haggerty et al.*, 2015]. For better understanding of how electrons are heated during asymmetric reconnection, more detailed discussions on how and where electron heating occurs are needed.

A previous laboratory study of asymmetric reconnection [*Yoo et al.*, 2014a] showed that the measured 2-D electron temperature profile was different from that in relatively symmetric reconnection [*Yoo et al.*, 2014b]. In particular, electrons were also heated downstream near the low-density side separatrix for asymmetric reconnection, while the electron temperature peaked at the edge of the electron diffusion region for symmetric reconnection. Electromagnetic fluctuations whose characteristics were consistent with turbulence driven by lower hybrid drift instability (LHDI) were observed near the low-density side separatrices where strong density gradients exist [*Yoo et al.*, 2014a]. LHDI-driven fluctuations were also observed in relatively symmetric, antiparallel reconnection in Magnetic Reconnection Experiment (MRX) [*Ji et al.*, 2004], but it was concluded that they did not play an important role in broadening the current sheet layer [*Roytershteyn et al.*, 2013]. LHDI-driven fluctuations have been observed in many space observations near the magnetosphere-side (low-density side) separatrices [*Vaivads et al.*, 2004; *Mozer et al.*, 2011; *Pritchett et al.*, 2012; *Graham et al.*, 2014]. The amplitude of these fluctuations is larger than the reconnection electric field, and these wave activities have a strong correlation with increase of the parallel electron temperature ($T_{e||}$) [*Tang et al.*, 2013]. However, increase in $T_{e||}$ can be also caused by the parallel electric field on the low-density side [*Egedal et al.*, 2011; *Graham et al.*, 2014] and the role of LHDI-driven fluctuations on electron heating or acceleration is still unclear.

Studies of the energy inventory concern how much of the incoming magnetic energy is converted to different forms of outgoing energy such as enthalpy (thermal) and flow energy. The quantitative analysis of the energy inventory gives us a chance to evaluate the role of reconnection in electron and ion energization in magnetized plasmas. Because previous studies are limited to symmetric, antiparallel reconnection [*Aunai et al.*, 2011; *Eastwood et al.*, 2013b; *Yamada et al.*, 2014, 2015], it is important to discuss how the overall energy inventory during reconnection changes under different conditions such as with density asymmetry.

Here laboratory studies of electron heating and the energy inventory during asymmetric reconnection without a significant guide field are reported. Extended 2-D profiles of the electron temperature, density, and plasma potential are obtained in plasmas with the density ratio of about 8 across the current sheet. Numerical simulations and experimental measurements show that LHDI-driven fluctuations do not play a major role in electron energization but possibly in electron thermalization. After examining possible heating mechanisms, we find that electrons can be heated by the energy gain from the parallel electric field. On the other hand, a quantitative analysis of the profile of the electron energy gain, $\mathbf{J}_e \cdot \mathbf{E}$, shows that the energy gain is dominated by that associated with the diamagnetic current and the perpendicular electric field. However, the energy gain associated with the diamagnetic current does not directly contribute to electron heating. Furthermore, the dependence of average bulk electron heating on the incoming magnetic energy is measured and compared with the space data by *Phan et al.* [2013]. Finally, the overall energy inventory during asymmetric reconnection is presented in comparison with the symmetric case by *Yamada et al.* [2014].

2. Experimental Setup

These experiments were carried out at the Magnetic Reconnection Experiment (MRX) facility [*Yamada et al.*, 1997]. Figure 1a shows a toroidal cross section of MRX in the $R-Z$ plane. Since MRX has a cylindrical vacuum vessel, it is symmetrical along the toroidal (Y) direction. The two gray circles indicate cross sections of the

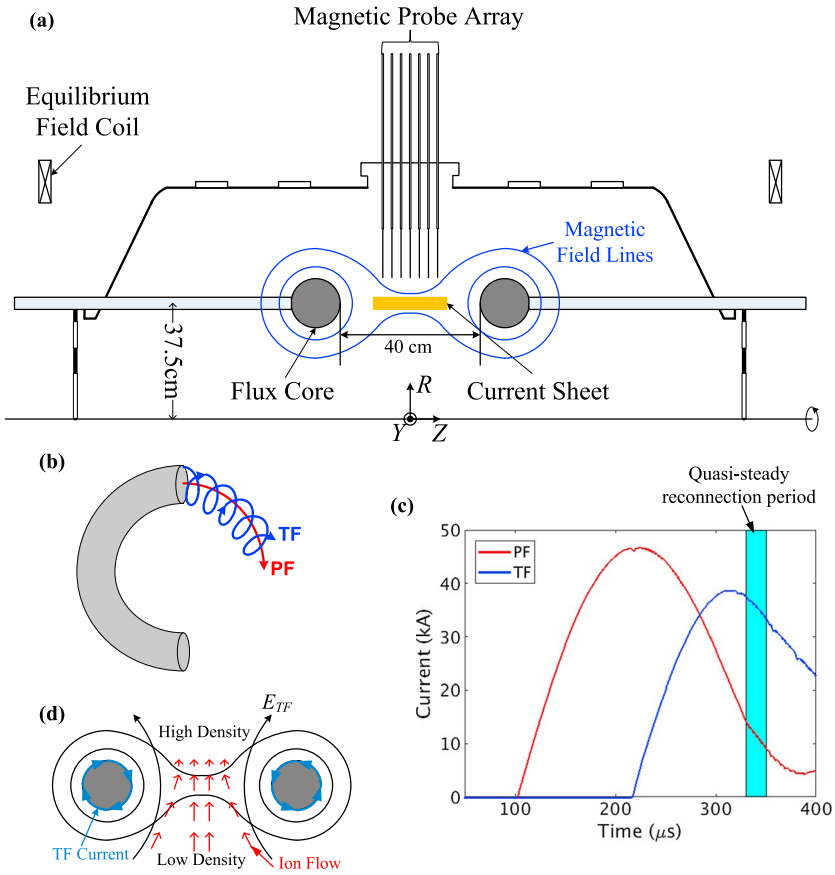

Figure 1. Experimental setup in MRX. (a) Toroidal cross section of MRX. The gray circles indicate flux cores that have two independent sets of coils: TF and PF coils. The blue lines demonstrate sample magnetic field lines and the orange box illustrates the current sheet. The coordinate system for the experiment is also shown. The magnetic probe array, the main diagnostics of this study, is inserted radially to measure the detailed structure of the current sheet. The surface-to-surface distance between two flux cores is set to be 40 cm for this study. (b) Coil windings of the flux core. The PF coils are wound toroidally, while TF coils are would poloidally. (c) Profile of the PF (red) coil current and TF (blue) coil current. Magnetic reconnection is driven by ramping down the PF current. The current of the TF coils is used to generate plasmas in the chamber. The quasi-steady reconnection period (t = 330–350 μs) where the reconnection rate stays relatively constant is indicated by a cyan box. (d) Schematic view of the ion dynamics during the plasma formation period. The blue arrows along the flux cores indicate the direction of the TF coil current. The red arrows between the flux cores stand for the ion flow vectors. Due to the inductive electric field from the increase TF coil current (E_{TF}), ions are transported to the outboard side ($R > 37.5$ cm), creating large density asymmetry.

"flux cores" inside which there are two independent sets of coils: poloidal field (PF) coils and toroidal field (TF) coils, as shown in Figure 1b. The PF coils are wound toroidally to generate the X line geometry at the middle of the MRX device and to drive magnetic reconnection. The TF coils are wound poloidally to inductively create the plasma around the flux cores. Typical current waveforms for the present experiment are shown in Figure 1c. First, the PF coils are energized to generate magnetic fields. Around the time the PF current reaches its maximum, the TF coils are energized. The time-varying TF current generates a strong poloidal inductive electric field around flux cores, thereby breaking down the gas which is puffed into the vessel before the PF coils are energized. We study physics of reconnection during the quasi-steady reconnection period over which the reconnection rate is relatively constant. The quasi-steady period is indicated with a cyan box in Figure 1c. As shown in Figure 1c, the PF current decreases during the quasi-steady period, such that the field lines are "pulled" back to the PF coils. As a result, the current sheet during this period is elongated along the Z direction, such that the radial (R) direction is normal to the current sheet and the toroidal (Y) direction is out-of-plane. For this experimental campaign, no external guide field is applied but there is a slight (less than 10% of the reconnecting magnetic field) guide field that is a remnant from the plasma formation.

During the plasma formation period, this inductive electric field from the TF coils generates a density asymmetry along the R direction [*Yoo et al.*, 2014a]. As shown in Figure 1d, the direction of the inductive electric field is radially outward for this study, such that ions are transported along the electric field direction. As a result, the density on the outboard ($R > 37.5$ cm) side becomes larger than that on the inboard ($R < 37.5$ cm) side. The density asymmetry formed during the plasma formation decays over tens of Alfvén times. By changing the TF current waveform, the gas species, and the fill pressure, the density asymmetry during the quasi-steady reconnection period can be controlled. We use helium plasmas for this study since they have generally larger density asymmetry, compared to hydrogen or deuterium plasmas. Moreover, they facilitate ion temperature measurements with an ion dynamics spectroscopy probe (IDSP) [*Fiksel et al.*, 1998], which are important for the energy inventory for ions. The details on the ion temperature measurement are described in *Yoo et al.* [2013, 2014b].

The main diagnostic for this study is a 2-D magnetic probe array, which consists of about 250 miniature pickup coils. The number of measurement points in the $R-Z$ plane is 91 for B_Z and B_Y, and 63 for B_R. The resolution along the Z direction is 3 cm and the maximum resolution in the R direction is 0.6 cm. It provides the time evolution of the magnetic field ($\mathbf{B}$), from which the current density ($\mathbf{J} = \nabla \times \mathbf{B}/\mu_0$) as well as the out-of-plane reconnection electric field ($E_Y = -(1/2\pi R)\mathrm{d}\psi/\mathrm{d}t$; ψ is the poloidal magnetic flux) can be obtained. Triple Langmuir probes [*Chen and Sekiguchi*, 1965] are used to measure the electron density (n_e) and temperature (T_e). The plasma potential (Φ_p) is obtained from the profiles of the floating potential and electron temperature [*Yoo et al.*, 2013]. Mach probes are used to measure the ion flow vector ($\mathbf{V}_i$) due to their better spatial and temporal resolutions, compared to the IDSP. The ion temperature profile is measured by an IDSP with 10 μs of the exposure time and 4 cm of the distance between the lens and the view dump. A fluctuation probe is used to measure all three components of magnetic fluctuations as well as the out-of-plane component of electrostatic fluctuations in the floating potential up to 20 MHz [*Carter et al.*, 2001].

New sets of 2-D profiles of key plasma parameters such as n_e, T_e, Φ_p, $\mathbf{V}_i$, $\mathbf{V}_e$, and T_i are obtained for this study by extensive $R-Z$ scans. Compared to profiles for the previous study by *Yoo et al.* [2014a], these profiles cover the region further downstream, which is $\sim 2d_i$ away from the X line, where $d_i = c/\omega_{pi} \approx 7.5$ cm is the ion skin depth based on the density at the X line. Here ω_{pi} is the ion plasma frequency. The extension of the measurement area is necessary for comparison to previous studies of electron heating [*Yoo et al.*, 2014b] and energy inventory [*Yamada et al.*, 2014] for symmetric, antiparallel reconnection. The reproducibility of discharges is monitored by data from the 2-D magnetic array and three reference Langmuir probes. The criteria include the location of the X line, electron densities, density asymmetry, and plasma current. The X line position of selected discharges resides in the region $37 \le R \le 38$ cm and $-1.5 \le Z \le 1.5$ cm. About 35% of 2200 discharges are used to produce 2-D profiles. At each measurement point, 7–10 similar discharges are obtained for meaningful statistical analyses. A typical standard deviation of important physical quantities such as the electron density is 10–15% of the mean value. The radial distance between two measurement points is typically 1 cm for Langmuir and Mach probes and 2 cm for the IDSP.

3. Features of Asymmetric Reconnection

Figure 2a presents the 2-D profile of the electron density, which shows the clear density asymmetry across the current sheet. The color contours show the density profile and the black lines are the contours of the poloidal flux (ψ) that represent magnetic field lines. The location of the X line is $(R, Z) = (37.5, 0)$ cm. The density on the outboard side ($R = 43.5$ cm) is about $n_1 \approx 4.0 \times 10^{13}/\mathrm{cm}^3$, while that on the inboard side ($R = 31.5$ cm) is about $n_2 \approx 0.5 \times 10^{13}/\mathrm{cm}^3$, which makes the upstream density ratio, n_1/n_2, is about 8. From now on, the subscript 1 denotes upstream quantities on the high-density (outboard, $R = 43.5$ cm) side, and the subscript 2 means those on the low-density (inboard, $R = 31.5$ cm) side. In the downstream region, the density becomes higher ($\sim 8.0 \times 10^{13}/\mathrm{cm}^3$), which is caused by density pileup due to the existence of the flux cores. The strength of the reconnecting field component on both sides is $B_1 = 145$ Gauss and $B_2 = 168$ Gauss, respectively. The Lundquist number and normalized system size (L/d_i; L is the system size) based on high-density side parameters are about 200 and 6, while those based on low-density side parameters are about 600 and 2, respectively. With these plasma parameters, the plasma for this study is in the single X line collisionless regime of the reconnection phase diagram [*Ji and Daughton*, 2011; *Le et al.*, 2015]. The surface-to-surface distance between the two flux cores for this study is 40 cm, as illustrated in Figure 1a.

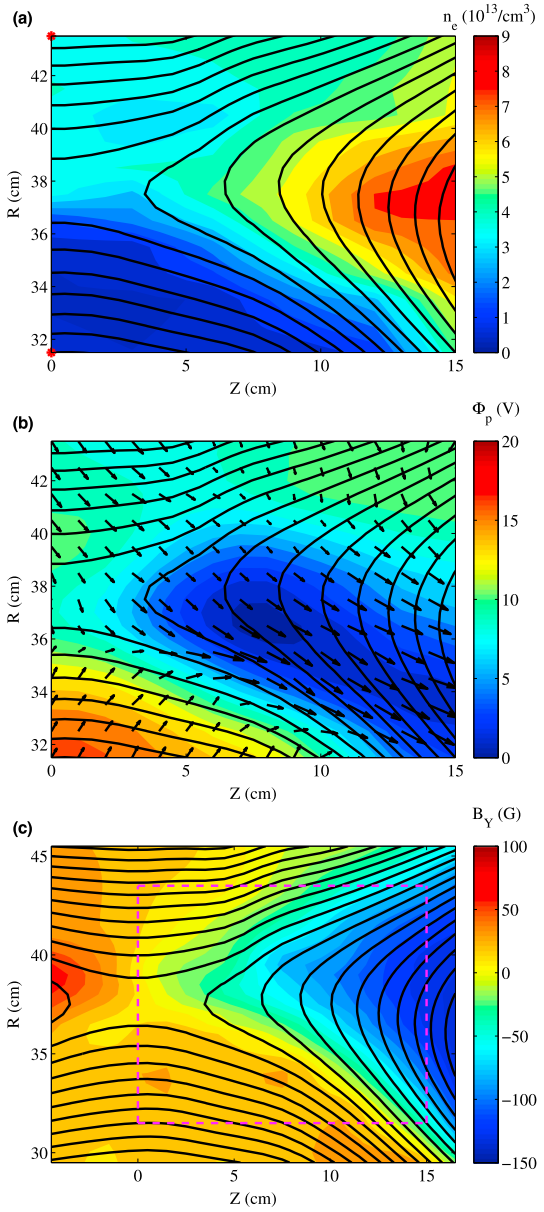

Figure 2. Features of asymmetric reconnection in MRX. (a) Electron density profile measure by a Langmuir probe. The black lines indicate the poloidal flux contours, which represent magnetic field lines. The measured profile shows a large density asymmetry across the current sheet and significant density pileup in the exhaust region. Two locations to define upstream quantities are marked with red asterisks. Quantities on the high-density side ($R = 43.5$ cm) and low-density side ($R - 31.5$ cm) are indicated by subscript 1 and 2, respectively. The upstream density ratio, n_1/n_2, is about 8. Note that large density gradients form near the low-density side separatrices. (b) Plasma potential profile together with in-plane ion flow vectors (arrows). Large potential drops (15–20 V) across the separatrices, which are observed during symmetric reconnection [*Yoo et al.*, 2013], exist only on the low-density side. Due to this large potential change, most ions from the high-density side remain in the exhaust region, generating large density gradients near the low-density side separatrices, as shown in Figure 2a. The ion flow pattern also shows that ion inflow stagnation points exist around the low-density side separatrices, supporting the above argument. (c) Out-of-plane magnetic field profile. The quadrupole profile during symmetric reconnection becomes bipolar during asymmetric reconnection. The magenta dashed lines indicate the region where the energy inventory in section 6 is carried out. All the relevant physical quantities are measured in the region.

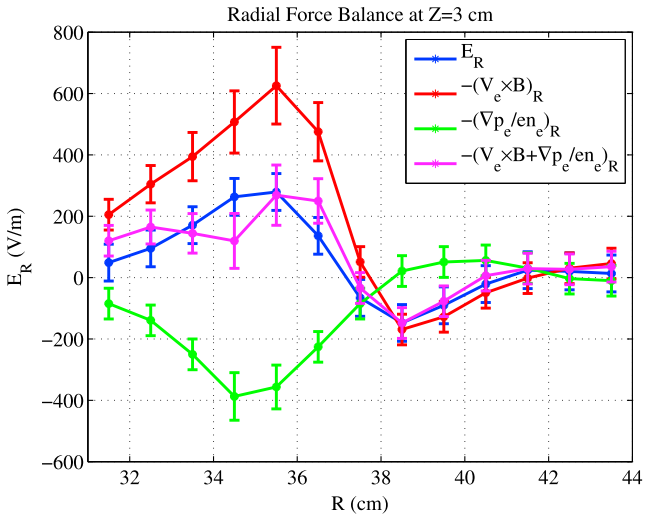

Figure 3. Radial force balance at $Z = 3$ cm. The measured radial electric field is balanced by the sum of the electron Lorentz force term and the pressure gradient term. Due to the large density asymmetry, the electron Lorentz force term is large only on the low-density side. The pressure gradient term decreases asymmetry in the radial electric field.

These 2-D density profiles show an important feature of asymmetric reconnection: large density gradients exist near the low-density side separatrices [*Pritchett*, 2008; *Tanaka et al.*, 2008; *Malakit et al.*, 2010; *Khotyaintsev et al.*, 2006]. This means that the plasma, especially ions, on the high-density side does not easily cross the low-density side separatrices. This limited ion transportation from the high-density to the low-density side is related to the electrostatic potential barrier near the low-density side separatrices.

Color contours of Figure 2b show the in-plane plasma potential profile, which shows large potential change near the low-density side separatrices, which agrees with space observations and simulations [*Mozer et al.*, 2008a, 2008b; *Pritchett*, 2008; *Tanaka et al.*, 2008; *Malakit et al.*, 2010]. Due to the large potential barrier, most ions from the high-density side do not move across the low-density side separatrices, generating large density gradients there. This asymmetric plasma potential can be explained by the electron force balance [*Pritchett*, 2008; *Yoo et al.*, 2013]. As shown in Figure 3, the in-plane electric field balances the sum of the electron Lorentz force ($\mathbf{V}_e \times \mathbf{B}$) and the pressure gradient. Due to the large density asymmetry, the Lorentz force is only significant on the low-density side, where the out-of-plane electron drift velocity (V_{eY}) is large. In contrary, the drift velocity on the high-density side is much smaller. As a result, only the low-density side has a large in-plane electric field, making the potential profile asymmetric as shown in Figure 2b. The large electron pressure gradient near the low-density side separatrices prevents the further asymmetry in the potential profile by reducing the $\mathbf{V}_e \times \mathbf{B}$ contribution, as shown in Figure 3.

Black arrows in Figure 2b show the in-plane ion flow pattern. Consistent with previous studies [*Cassak and Shay*, 2007; *Pritchett*, 2008; *Yoo et al.*, 2014a], the inflow ion stagnation point where $V_{iR} = 0$ is shifted toward the low-density side ($R = 36$ cm). This inflow stagnation shift is caused by the imbalance of the incoming mass flux due to the density asymmetry [*Cassak and Shay*, 2007]. The ion outflow is also asymmetric, as the location with the highest outflow velocity is shifted toward the low-density side [*Pritchett*, 2008; *Yoo et al.*, 2014a]. This outflow pattern is also related to the asymmetric in-plane potential profile. The highest ion outflow velocity is due to ions accelerated by the large in-plane electric field near the low-density side separatrices. These ions include ones from the low-density side as well as some from the high-density side that have moved across the separatrices during their meandering motions. Since a relative population of these ions is larger near the low-density side separatrices, the ion outflow is highest there.

The out-of-plane Hall magnetic field is also asymmetric as shown in Figure 2c, which is also consistent with previous studies [*Mozer et al.*, 2008a, 2008b; *Pritchett*, 2008; *Tanaka et al.*, 2008; *Malakit et al.*, 2010; *Yoo et al.*, 2014a]. The quadrupole profile of the Hall magnetic field becomes nearly bipolar with a much less strength on the low-density side. As explained in *Yoo et al.* [2014a], this is related with the Hall term in the generalized Ohm's law. The 2-D profile of the reconnection electric field (E_{rec}) (not shown) is relatively uniform. In upstream regions, this reconnection electric field is balanced by the $\mathbf{J} \times \mathbf{B}$ Hall term. As a result, we have

$$E_{\mathrm{rec}} \approx -\frac{J_1 B_1}{e n_1} \approx -\frac{J_2 B_2}{e n_2}. \quad (1)$$

Because asymmetry in the reconnecting magnetic field is not as strong as that in the density, the Hall current of the high-density side J_1 is larger than J_2 by about the density ratio. Sine the Hall current is responsible for the out-of-plane magnetic field, the Hall magnetic field is stronger on the high-density side.

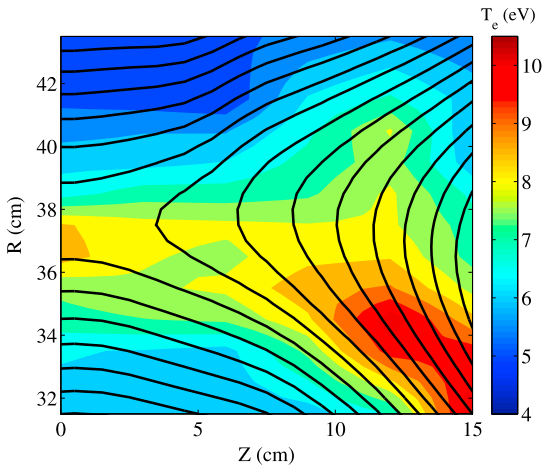

Figure 4. Electron temperature profile during asymmetric reconnection in MRX. Similar to the symmetric case, electrons are heated near the X line. However, unlike the symmetric case, electrons are further heated in the exhaust region near the low-density side separatrices is observed.

4. Asymmetric Electron Heating

Figure 4 shows the 2-D electron temperature profile. There are two major differences between this profile and one for symmetric reconnection in *Yoo et al.* [2014b]. First, electrons are further heated in the downstream region; the electron temperature at the X line is about 8 eV, while it reaches about 10 eV in the downstream region. Second, the electron temperature in the downstream region is fairly asymmetric; it has higher temperature on the low-density side. This profile raises an interesting question: why are electrons further heated downstream in this plasma on the low-density side?

4.1. LHDI-Driven Fluctuations

One candidate is electron heating by LHDI-driven fluctuations, since they are observed consistently near the low-density side separatrices where strong density gradients generate LHDI [*Yoo et al.*, 2014a]. In MRX, fluctuations in both electric and magnetic field in the frequency range below the lower hybrid frequency, $f_{LH} \lesssim 3$ MHz, are observed. Typical amplitudes of LHDI-driven fluctuations in MRX are 200 V/m in the electric field and 5–7 Gauss in the magnetic field. For comparison, the reconnection electric field is about 100 V/m and the shoulder value of the reconnecting magnetic field component is about 100 Gauss. Here the shoulder value means the value just outside the current sheet. The corresponding energy density of these fluctuations is 0.1–0.2 J/m^3, which is small compared to the electron internal energy density, $u_e = 1.5 n_e T_e = 8$–200 J/m^3.

Since it is difficult to understand microphysics of interactions between electrons and high-frequency fluctuations, data from numerical simulations are analyzed to see the effects of LHDI-driven fluctuations on electron heating. A high-performance particle-in-cell (PIC) code, VPIC [*Bowers et al.*, 2008] is used. Initial conditions for the magnetic field, the density profile, and distribution functions are described in *Roytershteyn et al.* [2012]. The reconnection is driven by applying an out-of-plane electric field [*Roytershteyn et al.*, 2012]. The mass ratio, m_i/m_e, is 900, which is large enough to see the dynamics of LHDI [*Daughton*, 2003]. The upstream density ratio, n_1/n_2 is 10, which is similar to the experimental value of 8. No temperature asymmetry is applied in simulations. The plasma β on the high-density side is 0.5, which is also similar to the experimental value ($\beta = 0.6$, d_i away from the center of the current sheet). Other numerical parameters are $T_i/T_e = 1$, $v_{the}/c = 0.2$, and $\omega_{pe}/\omega_{ce} = 1.75$ on the high-density side. It is worth noting that the electron temperature is set to be artificially high to save the computation time. The spatial domain is $10d_i \times 10d_i$ with 1024^2 cells for the 2-D case and $10d_i \times 10d_i \times 3d_i$ with $1024^2 \times 320$ cells for the 3-D case. The initial number of particles is about 6.3×10^8 for the 2-D case, while it is about 2.0×10^{11} for the 3-D case. No guide field is applied in these simulations as in the experiment. Here v_{the} is the electron thermal velocity, ω_{pe} is the electron plasma frequency, and $\omega_{ce} \equiv eB/m_e$ is the electron cyclotron frequency. The coordinate system for the simulation data presented below is x for the normal direction to the current sheet, y for the out-of-plane direction, and z for the outflow direction. Simulations also show typical features of asymmetric reconnection such as bipolar out-of-plane magnetic field, asymmetric in-plane electric field, and shifted ion stagnation point, which are in qualitative agreement with MRX results.

Figures 5a and 5c show the electron temperature profile during steady state reconnection ($t \sim 50/\omega_{ci}$; ω_{ci} is the ion cyclotron frequency) in the 2-D and 3-D simulation, respectively. The electron temperature is defined as $T_e = (p_{e,xx} + p_{e,yy} + p_{e,zz})/n_e$, where $p_{e,ij}$ denotes the component of the electron pressure tensor, $\mathbf{P}_e$. For the 3-D case, the temperature is averaged over the out-of-plane direction. Due to the lack of the third dimension, the 2-D simulation does not have LHDI dynamics. If there is significant electron heating by LHDI-driven fluctuations, the electron temperature profile will be different because both cases have the same initial conditions. Although there is strong development of LHDI around the low-density side separatrices for the

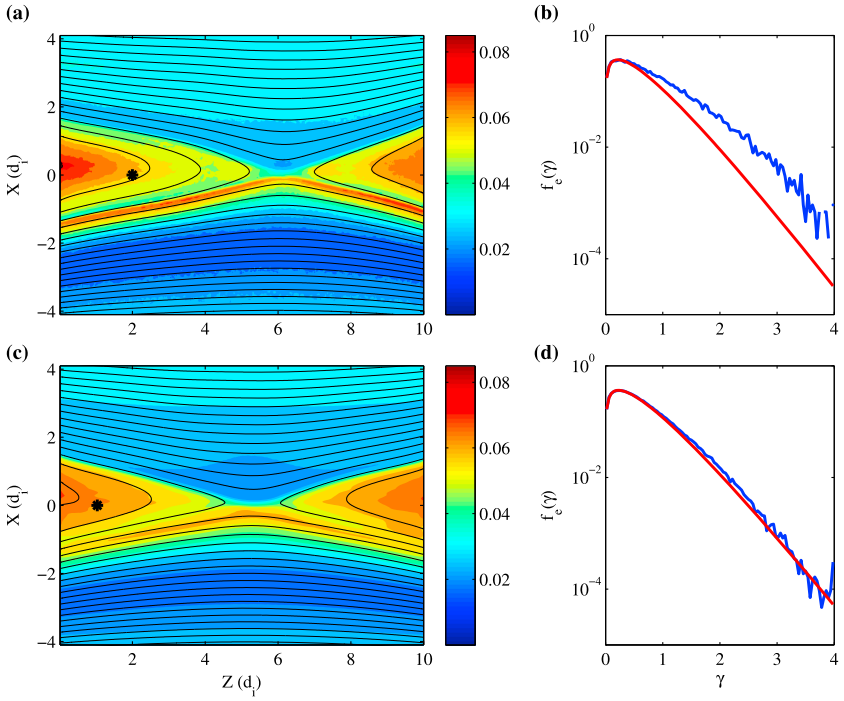

Figure 5. Electron temperature profiles and distribution functions in the exhaust region in the (a, b) 2-D and (c, d) 3-D simulation. The color contours in Figures 5a and 5c indicate the electron temperature, $T_e = (p_{e,xx} + p_{e,yy} + p_{e,zz})/n_e$. The temperature is normalized by $m_e c^2$. In Figures 5b and 5d, the blue lines show the electron energy distribution in the exhaust region, while the red lines indicate fittings of the distribution functions to the relativistic Maxwellian distribution. The location where the distribution function is evaluated is marked by a black asterisk in Figures 5a and 5c. In the 3-D simulation, LHDI-driven fluctuations exist [*Roytershteyn et al.*, 2012] but the average amount of electron temperature increase in the exhaust region is similar to that in the 2-D simulation. The electron energy distribution function in the exhaust region, on the other hand, is different, showing more electron thermalization in the 3-D simulation, which indicates LHDI-driven fluctuations may contribute to electron thermalization. Here $\gamma = 1/\sqrt{1 - v^2/c^2}$ is the Lorentz factor, representing the energy of electrons.

3-D case, the electron temperature profiles are generally similar especially in the exhaust region over the steady state reconnection period, which indicates that there is no significant energy flow from LHDI to electrons. The band of a high temperature region near the low-density side separatrices is caused by the electron energization by the parallel electric field [*Egedal et al.*, 2011] and exists in both simulations but its width is much sharper in the 2-D case. The limitation of these simulations regarding the artificial high electron temperature has to be mentioned, since the high electron temperature can prevent development of the Debye-scale dynamics [*Jara-Almonte et al.*, 2014]. It will be a interesting study the impact of LHDI on electron energization, when the electron temperature is closer to the realistic value.

Electron energy distribution functions, on the other hand, show noticeable differences between two simulations. Figures 5b and 5d present a sample electron energy distribution function $f_e(\gamma)$ from 2-D and 3-D simulations, respectively. Here $\gamma = 1/\sqrt{1 - v^2/c^2}$ is the Lorentz factor. The location where the distribution functions are obtained is marked by a black asterisk in Figures 5a and 5c. The size of the area (volume) for sampling is a $2d_e$ square (cube). The blue lines indicate the distribution function in simulations, while the red curves are the fitting of the distribution functions to the relativistic Maxwellian distribution. The 2-D case in Figure 5b shows more energetic population than the 3-D case, which is valid throughout the exhaust region. This indicates that LHDI may play a role in electron thermalization, although further studies of interactions between LHDI and electrons are required to confirm this argument.

The relevance of these simulations to the observed electron heating in MRX can be challenged. In particular, the electron dynamics and heat transport may be quite different due to the artificially high v_{the}/c and low ω_{pe}/ω_{ce} in simulations. However, electron heating by LHDI is not conclusively supported by experiments, either. There is no strong correlation between the downstream electron temperature at $Z = 7.5$ cm and the amplitude of LHDI-driven fluctuations at $Z = 1.5$ cm, as shown in Figure 6. The correlation coefficient between

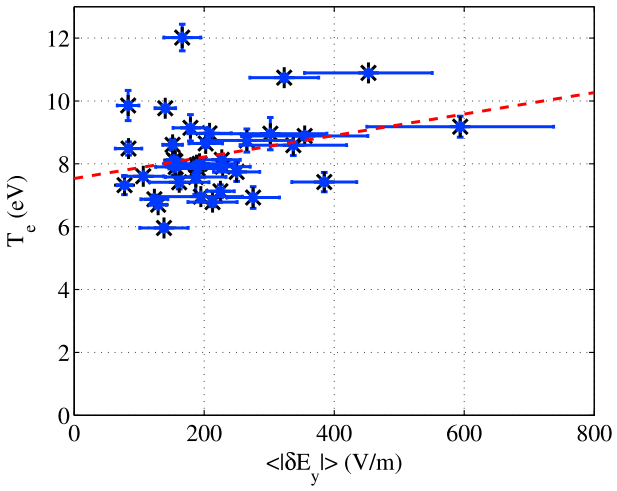

Figure 6. The average electron temperature (T_e) in the exhaust region ($Z = 7.5$ cm) as a function of the average amplitude ($\langle|\delta E_y|\rangle$) of LHDI-driven fluctuations at $Z = 1.5$ cm. The red dashed line indicates the fit of data to a linear function. The correlation coefficient between $\langle|\delta E_y|\rangle$ and T_e is 0.29 with a probability value for the null hypothesis of 0.086, which means relatively weak correlation and weak statistical significance.

$\langle|\delta E_y|\rangle$ and T_e is 0.29, which means a relatively weak correlation between two quantities. The probability value for the null hypothesis is 0.086, which is larger than the usual cutoff value of 0.05, indicating that the positive correlation is not statistically significant. Even if we believe the positive correlation, the expected average temperature increase in the exhaust region with the average value of $\langle|\delta E_y|\rangle \sim 210$ V/m is about 0.7 eV, which is smaller than electron heating ΔT_e of about 3 eV in these discharges. Here ΔT_e is the average electron temperature increase from the high-density side upstream region (~5 eV) to the measured downstream location at $Z = 7.5$ cm (~8.3 eV). Although this correlation study does not definitively deny the role of LHDI in electron heating, it supports the assertion that LHDI is not the major mechanism for electron heating in MRX.

4.2. Electron Energization by Single-Particle Motion

Since the electron temperature is a fluid quantity, a fluid equation such as the electron energy transport equation (equation (9)) is preferred for discussion of local electron heating. However, it is difficult to measure all of the required fluid quantities such as the pressure tensor and microscopic heat flux in the experiment. On the other hand, single-particle dynamics is easy to discuss because the mean field profiles are already known. Energization by the single-particle motion does not guarantee the local electron heating, since there are other fluid effects such as compression and heat conduction. However, it can tell where and how a thermal electron is energized, which will help identify a possible heating mechanism.

A candidate for electron energization by a single-particle motion is the polarization drift from the spatially varying Hall fields. As shown in Figures 2b and 2c, both the in-plain electric field and the out-of-plane magnetic field changes rapidly in space near the low-density side separatrices. With these sharp changes in the fields, the perpendicular energy of electrons can change while they do the gyromotion. This electron energization is related to the polarization drift, which is given by

$$\mathbf{v}_{\mathrm{ep}} = \frac{\mathbf{b}}{\omega_{\mathrm{ce}}} \times \frac{\mathrm{d}\mathbf{V}_{E\times B}}{\mathrm{d}t}, \tag{2}$$

where $\mathbf{b}$ is the unit vector along the magnetic field, and $\mathbf{V}_{E\times B}$ is the $\mathbf{E}\times\mathbf{B}$ velocity. The polarization drift usually means the drift responding the time-varying field but it can be generalized to include drifts caused by spatially varying fields.

The electron energy gain by the polarization drift is estimated to be negligible. Ignoring the parallel motion and time variations, the total derivative $\mathrm{d}/\mathrm{d}t \sim V_{E\times B}/L_\perp$, since the leading order drift velocity perpendicular to the magnetic field is $V_{E\times B}$. Here $L_\perp$ is the length scale along the perpendicular direction. Then, $\mathbf{v}_{\mathrm{ep}}$ can be approximated as $v_{\mathrm{ep}} \sim V_{E\times B}^2/\omega_{\mathrm{ce}}L_\perp$. The energy gain of an electron due to the generalized polarization drift is

$$\Delta\left(\frac{m_e v_e^2}{2}\right) = -e\Delta t\mathbf{E}_\perp \cdot \mathbf{v}_{\mathrm{ep}} \sim \frac{e\Delta t E_\perp V_{E\times B}^2}{\omega_{\mathrm{ce}}L_\perp}, \tag{3}$$

where Δt is the transit time for an electron to pass through the low-density side separatrices. If the parallel motion is ignored, $\Delta t \sim L_{\mathrm{sep}}/V_{E\times B}$, where L_{sep} is the width of the separatrix region where strong variation of the electric field exists. As a result, the energy gain is

$$\Delta\left(\frac{m_e v_e^2}{2}\right) \sim \frac{eE_\perp V_{E\times B} L_{\mathrm{sep}}}{\omega_{\mathrm{ce}}L_\perp}. \tag{4}$$

With the measured values of $E_\perp \lesssim 400$ V/m, $V_{E\times B} \lesssim 3\times10^4$ m/s, $\omega_{ce} \gtrsim 2\times10^9$ rad/s, $L_{sep} \lesssim 5$ cm, and $L_\perp \gtrsim 0.5$ cm, the energy gain is less than 0.01 eV, which is negligible.

The energy gain by the polarization drift is negligible, even if the parallel motion is considered. In this case, $\mathrm{d}/\mathrm{d}t \sim v_{e||}/L_{||}$, where $v_{e||}$ is the parallel electron velocity and $L_{||} \sim 5$ cm is the scale length along the magnetic field. A typical parallel velocity is the electron thermal velocity, which is about 1×10^6 m/s. The transit time, Δt, becomes $L/v_{e||}$, where $L \sim 15$ cm is the total travel distance of the electron along the magnetic field. Then, the estimated energy gain is

$$\Delta\left(\frac{m_e v_e^2}{2}\right) \sim \frac{eE_\perp V_{E\times B} L}{\omega_{ce} L_{||}}. \tag{5}$$

Again, the electron energy gain is estimated to be smaller than 0.01 eV.

Electron energization by other drift motions such as the grad B drift and curvature drift is also negligible near the low-density side separatrices. Energization by the grad B drift ($v_{e\nabla B} \equiv -(mv_{e\perp}^2/2e)\mathbf{B}\times\nabla B/B^3$) is related to the conservation of $\mu \equiv m_e v_{e\perp}^2/B$ [*Dahlin et al.*, 2014]. Because the magnetic field strength decreases downstream, the grad B drift makes electrons lose the perpendicular energy as they move across the separatrices. The energization by the curvature drift, which is related to the conservation of the parallel action ($J \equiv \int v_{e||}\mathrm{d}l$) [*Dahlin et al.*, 2014], is also not significant at least near the low-density side separatrices. As shown in Figure 4, the curvature of the magnetic field is small where electron heating is observed. Moreover, there is no noticeable electron heating near the midplane ($R \sim 38$ cm) where the curvature of the magnetic field is maximum.

The final candidate for electron heating is the direct electron energization by the parallel electric field [*Egedal et al.*, 2011]. The electron energy increase by the parallel electric field is described by

$$\frac{\mathrm{d}}{\mathrm{d}t}\left(\frac{m_e v_{e||}^2}{2}\right) = -eE_{||}v_{e||}, \tag{6}$$

where $E_{||}$ is the parallel electric field. If the transit time for electrons to pass the separatrix region is based on the perpendicular $\mathbf{E}\times\mathbf{B}$ motion ($\sim1\times10^4$ m/s) and the width of the separatrix region (~3 cm) where the parallel electric field exists, it is about 3 μs. With $E_{||}$ of about 40 V/m, which is the measured value near the low-density side separatrices, electrons can obtain more than 140 eV of energy within 1 μs. In reality, however, the electron energy gain is limited by the parallel motion and collisions. It should be also mentioned that the error bars of the parallel electric field measurement are large ($\sim$20 V/m) since its magnitude is much smaller than the local electric field ($\sim$400 V/m) and errors come from both electric field and magnetic field measurements.

The parallel motion of electrons significantly decreases the amount of electron energy gain. Once they are accelerated by the parallel electric field they will quickly flow out along the magnetic field, such that they have a limited time for acceleration. For example, a typical electron around $(R, Z) = (36, 5)$ cm in Figure 4 will move out of the reconnection region along the magnetic field before they reach the exhaust region by the $\mathbf{E}\times\mathbf{B}$ motion. With the electron thermal velocity of $\sim1\times10^6$ m/s and the travel distance of about 15 cm along the magnetic field, it takes about 0.11 μs for the electron to move out of the ion diffusion region. With this transition time, the average energy gain of electrons is about 5 eV.

Due to the existence of collisions in the MRX plasma, electrons are heated rather than accelerated. The mean free path of electrons near the low-density side separatrices is about 4 cm, so electrons can be thermalized before they move away from the reconnection region. The amount of the average energy gain from the parallel electric field within a collision time is about 2 eV, which is enough to explain the observed electron heating. We have also verified that there is no significant tail population in the exhaust region by measuring the electron energy distribution with an electron energy analyzer [*Na et al.*, 2017].

It is also worth noting that the direction of the parallel electric field in the exhaust region near the low-density side separatrix $(R, Z) \approx (34, 12)$ cm is different from the theoretical expectation in *Egedal et al.* [2011]. Since the parallel electric field is sustained by the pressure gradient along the magnetic field, the direction is the opposite to the pressure gradient, i.e., $E_{||} \equiv \mathbf{b}\cdot\mathbf{E} \approx -\nabla_{||}p_e/en_e$. The newly reconnected field line in the exhaust region connects high-density side to the low-density side, there is generally a pressure gradient along the field line during asymmetric reconnection. As a result, the direction of the parallel electric field in the exhaust

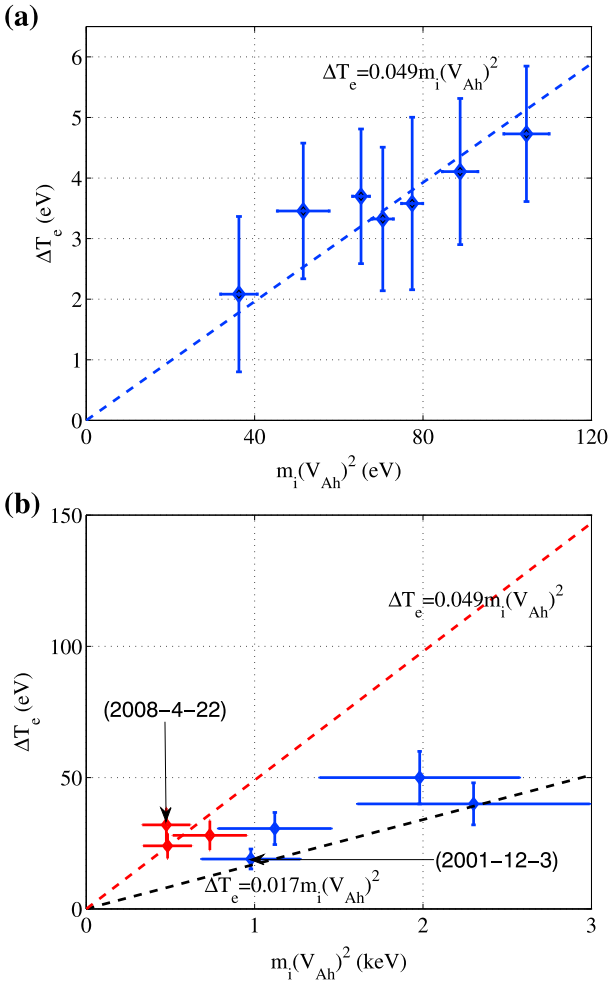

Figure 7. Average bulk electron heating (ΔT_e) versus the incoming magnetic energy per an electron/ion pair ($m_i V_{Ah}^2$) for (a) MRX measurements and for (b) seven Cluster events. The average electron heating is proportional to $m_i V_{Ah}^2$ in MRX but the scaling exceeds that of *Phan et al.* [2013]. Among seven Cluster events, there are three events marked with a red circle which is close to the MRX scaling (marked by the red dashed line). Those events are identified as crossings near the X line.

region is toward the X line near the high-density side and toward the exhaust region near the low-density side (see Figure 5 of *Egedal et al.* [2011]). However, in MRX, the electron pressure close to the flux cores ($Z = 15$ cm) is high due to the boundary conditions from the flux cores, such that the direction of the parallel electric field there is toward X line.

This electron heating by the parallel electric field may explain the asymmetric electron temperature. The magnitude of the parallel electric field near the high-density-side separatrices is much smaller (~10 V/m), because the average density is high and the pressure gradient is smaller. The mean free path of electrons is also shorter (~2 cm), which further limits the electron energy gain. Thus, electron heating by the parallel electric field is stronger near the low-density side separatrices.

4.3. Scaling of Average Bulk Electron Heating

The dependance of the average electron heating on the incoming magnetic energy is checked in this laboratory plasma. As shown in Figure 7a, the average bulk electron heating is proportional to the incoming magnetic energy per an electron-ion pair, $m_i V_{Ah}^2 = B_1 B_2 (B_1 + B_2)/\mu_0 (n_1 B_2 + n_2 B_1)$, which is consistent with space observations [*Phan et al.*, 2013]. Here V_{Ah} is the hybrid Alfvén velocity [*Cassak and Shay*, 2007; *Phan et al.*, 2013], and ΔT_e is the difference between T_e averaged over the exhaust region (at $Z = 13.5$ cm) and T_e on the high-density side. This temperature increase can represent the amount of electron heating, since the electron temperature on the low-density side is usually only about 1–2 eV higher than on the high-density side, and density ratio is more than 5. To obtain different $m_i V_{Ah}^2$ values, the fill pressure of the helium gas and PF current waveform have varied. Table 1 summarizes important upstream parameters for each data point in Figure 7a. All quantities are averaged over 10–20 discharges and error bars in Figure 7a are standard deviations of the data set.

In MRX, the bulk electron heating is about 4.9% of the incoming magnetic energy, which is larger than the space observation (~1.7%) [*Phan et al.*, 2013]. This scaling also exceeds the theoretical expectation based on the single-particle dynamics near the diffusion region [*Le et al.*, 2016]. This discrepancy can be caused by differences in the system size and boundary condition. Due to the limited system size ($L \sim 40$ cm $\sim 5\, d_i$), the measurement location in the exhaust region is only about $2d_i$ away from the X line. Since there is a significant electron energy gain near the X line (see Figure 8), the small separation can make the average electron temperature in the outflow region higher than when it is measured farther away from the X line where a relative population of electrons that pass the electron diffusion region is smaller. Additionally, as mentioned earlier, the boundary condition from the flux cores generates a different profile of the parallel electric field

Table 1. Upstream Plasma Parameters for Bulk Electron Heating Study in MRX[a]

	Quantity\Group						
	1	2	3	4	5	6	7
$m_i V_{Ah}^2$ (eV)	36.3	51.6	65.3	70.4	77.4	88.8	104.6
ΔT_e (eV)	2.1	3.5	3.7	3.3	3.6	4.1	4.7
n_1 (10^{19} /cm^3)	5.36	3.82	2.91	2.74	2.55	2.46	1.99
n_2 (10^{19} /cm^3)	0.22	0.41	0.44	0.52	0.39	0.28	0.37
n_1/n_2	24.5	9.3	6.6	5.3	6.5	8.7	5.4
B_1 (Gauss)	129	134	136	137	137	141	144
B_2 (Gauss)	179	178	176	186	184	194	186

[a]To obtain different upstream values, the gas fill pressure and PF current waveform have changed systematically. Values are averaged over 10–20 discharges. In all discharges, the guide field is negligible (less than 10 % of the reconnecting field component).

that helps energize electrons. There is also a contribution from the classical Ohmic heating, although it is small (<15%) compared to the total electron energy gain.

Figure 7b shows the dependence of ΔT_e on $m_i V_{Ah}^2$ for seven Cluster magnetopause crossings. Unlike *Phan et al.* [2013], we choose seven crossings regardless of clear existence of the ion jet, which means that these events may include crossings near the X line. To eliminate possible effects from the guide field, the chosen events have a guide field less than 30% of the reconnecting field component. Table 2 summarizes important upstream parameters for each data point in Figure 7b. Following *Phan et al.* [2013], the electron temperature increase, ΔT_e, is the difference in the average electron temperature between the magnetosheath and the exhaust region. The electron temperature is computed by fitting the electron distribution function to a double Gaussian function to include contributions from energetic electrons. As shown in Figure 7b, there are three events (marked with red circles) that exceed the scaling of 1.7% significantly. On the other hand, other four events (marked with blue circles) are closer to the 1.7% scaling in the space observation [*Phan et al.*, 2013].

Two of the above Cluster events marked with arrows and dates in Figure 7b have been previously discussed in literature *Graham et al.* [2014], *Retinò et al.* [2005], and *Tanaka et al.* [2008]. The event on 22 April 2008 is identified as a crossing near X line [*Graham et al.*, 2014]. We also follow the methodology described in *Argall* [2014] to estimate proximity to the X line for three events marked with red circles. Based on the profiles of the density, the reconnecting field (B_L), and the normal electric field (E_N), all three events with higher electron heating in Figure 7b show features of the crossing near the X line. On the other hand, the event on 3 December 2001 with a lower electron heating scaling is identified as a crossing away from the X line [*Tanaka et al.*, 2008; *Argall*, 2014]. These observations support the assertion that the average electron heating depends on the location of the measurement.

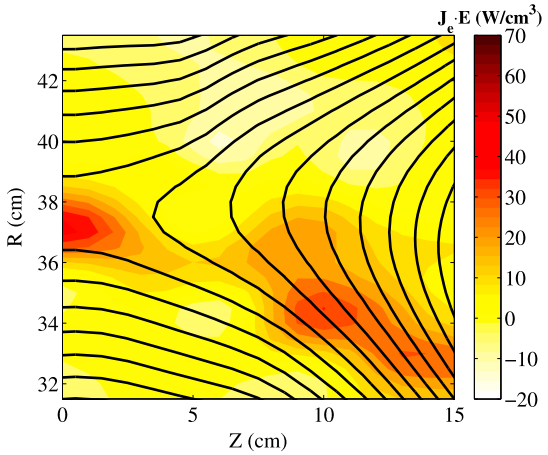

Figure 8. Profile of the electron energy gain from the electric field, $\mathbf{J}_e \cdot \mathbf{E}$. There is strong energy gain near X line, which is similar to the symmetric case. However, unlike the symmetric case, there is significant electron energy gain near the low-density side separatrices.

5. Electron Energy Gain From Electric Field

Figure 8 shows the $\mathbf{J}_e \cdot \mathbf{E}$ profile, which is the work done by the electric field on the electrons per unit time and unit volume. Positive $\mathbf{J}_e \cdot \mathbf{E}$ means that electrons gain energy from the field. Similar to the symmetric case, there is high energy gain near the X line but the location of the peak is slightly shifted to the

Table 2. Upstream Plasma Parameters for Seven Cluster Events[a]

	Quantity\Event						
	1	2	3	4	5	6	7
$m_i V_{Ah}^2$ (keV)	0.48	0.48	0.73	0.98	1.1	2.0	2.3
ΔT_e (eV)	32	24	28	19	30	50	40
n_1 (/cm^3)	31.0	9.1	14.2	19.2	111.5	55.8	41.3
n_2 (/cm^3)	0.14	0.21	0.67	0.19	0.05	3.3	0.63
n_1/n_2	221	43	21	101	2075	17	66
B_1 (nT)	32.7	22.3	27.5	40.2	92.7	98.9	83.2
B_2 (nT)	58.4	18.4	51.3	54.4	178.7	135.8	152

[a]In all events, the guide field is smaller than 30% of the reconnecting field component.

low-density side. Unlike the symmetric case, however, there is significant electron energy gain near the low-density side separatrices.

This additional electron energy gain is mostly related to the electron diamagnetic current ($\mathbf{J}_{eD}$), as shown in Figure 9. Due to the large pressure gradient, the out-of-plane component of the diamagnetic current is large near the low-density side separatrices. Here $\mathbf{J}_{eD} \equiv \mathbf{B} \times \nabla p_e / B^2$, where $p_e = n_e T_e$ is the electron pressure. We assume that the electron pressure is isotropic for simplicity.

As shown in Figure 9, the contribution from the parallel electric field ($J_{e||}E_{||}$) is small near the low-density side separatrices ($R \sim 32$ cm), compared to $\mathbf{J}_{eD} \cdot \mathbf{E} = \mathbf{J}_{eD} \cdot \mathbf{E}_\perp$. This large contribution from the perpendicular electric field to electron energization seems contradictory to the conclusion of section 4 where the role of the parallel electric field to electron heating is emphasized. However, the energy gain by $\mathbf{J}_{eD} \cdot \mathbf{E}$ does not directly contribute to electron heating. The diamagnetic current is related to the gyromotion of particles with a pressure gradient. The pressure gradient results in more particles in one direction than in the other, while they do the gyromotion, which appears as a fluid velocity. The current from this fluid velocity is called the diamagnetic current. The diamagnetic current appears only in the fluid picture, which means that it does not have the corresponding guiding center drift [*Goldston and Rutherford*, 2000]. Since the diamagnetic current is not related to any guiding center drift motion, $\mathbf{J}_{eD} \cdot \mathbf{E} > 0$ does not mean that $-e\mathbf{v}_{e,gc} \cdot \mathbf{E} > 0$, which is the necessary condition for a magnetized electron to be energized. Here $\mathbf{v}_{e,gc}$ means the velocity of the guiding center of an electron.

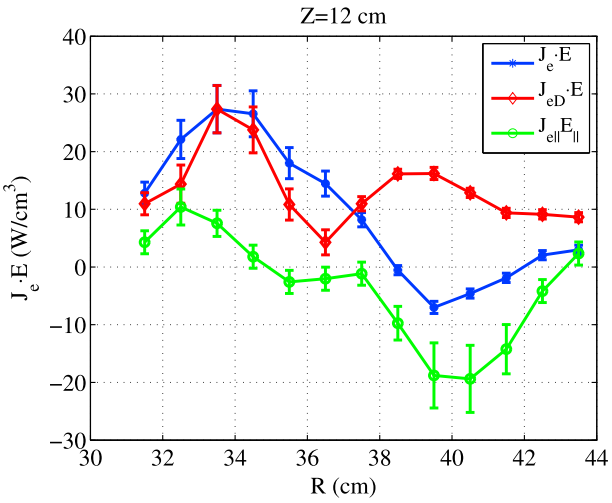

Figure 9. Profiles along the R direction at $Z = 12$ cm of the total electron energy gain ($\mathbf{J}_e \cdot \mathbf{E}$), electron energy gain associated with the diamagnetic current ($\mathbf{J}_{eD} \cdot \mathbf{E}$), and electron energy gain from the parallel electric field ($J_{e||}E_{||}$). The energy gain near the low-density side separatrices ($R \sim 33$ cm) is dominated by $\mathbf{J}_{eD} \cdot \mathbf{E}$.

The electron energy gain by $\mathbf{J}_{eD} \cdot \mathbf{E}$ is used to overcome the pressure difference across the separatrices. For better understanding of the role of $\mathbf{J}_{eD} \cdot \mathbf{E}$, it is useful to write the perpendicular electron current as [*Goldston and Rutherford*, 2000]

$$\mathbf{J}_{e\perp} \approx -en_e \mathbf{V}_{E\times B} + \frac{\mathbf{B} \times (\nabla \cdot \mathbf{P}_e)}{B^2}, \quad (7)$$

where $\mathbf{P}_e$ is the electron pressure tensor. Here the contributions from the electron resistivity ($\eta \mathbf{J}_e$) and the electron polarization drift are ignored. The first term on the right-hand side (RHS) is related to the $E \times B$ velocity. Although this term does not contribute to the electron energy gain ($\mathbf{J}_e \cdot \mathbf{E}$), it drives a fluid element from the upstream (low pressure) to the exhaust (high pressure)

region across the separatrices. This movement of the fluid element requires energy since the fluid element has to overcome the force from $\nabla \cdot \mathbf{P}_e$, which is

$$\mathbf{V}_{E\times B} \cdot (\nabla \cdot \mathbf{P}_e) = \frac{\mathbf{B} \times (\nabla \cdot \mathbf{P}_e)}{B^2} \cdot \mathbf{E} = \mathbf{J}_{e\perp} \cdot \mathbf{E}. \tag{8}$$

Assuming the isotropic electron pressure tensor ($\nabla \cdot \mathbf{P}_e = \nabla p_e$), $\mathbf{J}_{e\perp} \cdot \mathbf{E}$ is the same as $\mathbf{J}_{eD} \cdot \mathbf{E}$. Equation (8) shows that the electron energy gain related to the second term on the RHS of equation (7) provides the energy to complete the leading order $E \times B$ motion of the fluid element. This energy eventually contributes to the enthalpy increase in the exhaust region.

In the single-particle picture, electrons just move from the low pressure (upstream) to the high pressure (exhaust) region via the $E \times B$ drift, and there is no reason for additional energy gain if the only guiding center motion is the $E \times B$ drift. The force from the pressure gradient is a fluid concept and does not exist in the single-particle equation of motion. This argument is well valid in collisionless plasmas. Even in collisional plasmas, the single particle may "feel" the pressure via collisions with other particles but they will continue to do the $E \times B$ motion. Collisions may impact on the single-particle dynamics but conserve the energy.

The irrelevance of $\mathbf{J}_{eD} \cdot \mathbf{E}$ to electron heating can be also shown by the internal energy transport equation, which is [*Braginskii*, 1965]

$$\frac{\partial u_e}{\partial t} + \nabla \cdot (u_e \mathbf{V}_e) + \mathbf{P}_e : \nabla \mathbf{V}_e + \nabla \cdot \mathbf{q}_e = Q_e, \tag{9}$$

where $u_e = (3/2) n_e T_e$ is the electron internal energy, $\mathbf{P}_e$ is the electron pressure tensor, $\mathbf{q}_e$ is the electron heat flux, and Q_e is the heat generated by collisions with ions. Even though the diamagnetic drift contributes to Q_e by creating a relative velocity between electrons and ions, its contribution is small since $|\mathbf{V}_{eD}| \ll V_{e||}$, where $\mathbf{V}_{eD}$ is the electron diamagnetic drift velocity and $V_{e||}$ is the electron flow speed along the magnetic field. The energy gain from $\mathbf{J}_{eD} \cdot \mathbf{E}$ directly contributes neither to the compressional heating term ($\nabla \cdot (u_e \mathbf{V}_e)$) nor the viscous damping term ($\mathbf{P}_e : \nabla \mathbf{V}_e$).

6. Energy Inventory for Asymmetric Reconnection

The energy inventory concerns how much of the incoming magnetic energy is converted to different forms of energy such as the flow energy and enthalpy energy. Since the importance of magnetic reconnection is mostly from its ability to convert magnetic energy to plasma energy fast and efficiently, quantitative discussion on the overall energy inventory is important. For antiparallel, symmetric reconnection in MRX, the energy inventory shows that about 50% of the incoming magnetic energy is converted in the ion diffusion region and that the ion energy gain is about twice higher than the electron energy gain [*Yamada et al.*, 2014, 2015].

The methodology of the quantitative analysis of the energy inventory is the same as in *Yamada et al.* [2015]. The relevant incoming and outgoing energy fluxes at the boundary of a $\sim 2d_i \times 2d_i$ box are measured, which is indicated by the magenta dashed lines in Figure 2c. The measured energy fluxes include the Poynting ($\mathbf{E} \times \mathbf{B}/\mu_0$), electron/ion flow energy ($0.5 n_s m_s V_s^2 \mathbf{V}_s$; $s = e, i$), and electron/ion enthalpy ($2.5 n_s T_s \mathbf{V}_s$) fluxes. The electron/ion heat fluxes are estimated by formula in *Braginskii* [1965]. Electrons are assumed to be magnetized, which can be justified since the boundary is away from the electron diffusion region, while ions are assumed to be unmagnetized. Moreover, the change of the energy enclosed in the volume of the plasma specified by the boundary is also considered. For example, the thermal energy change of species s (ΔW_{Hs}) is given by

$$\Delta W_{Hs} = \int_{\mathcal{V}} \mathrm{d}^3 x \left[\frac{\partial}{\partial t} \left(\frac{3}{2} n_s T_s \right) + \nabla \cdot \left(\frac{5}{2} n_s T_s \mathbf{V}_s \right) \right], \tag{10}$$

where $\mathcal{V}$ is the volume enclosed by the boundary. The first term on the right-hand side represent the thermal energy change enclosed in the volume $\mathcal{V}$, while the second term means the difference between the outgoing and incoming enthalpy flux.

Figure 10 summarizes the energy inventory during asymmetric reconnection in MRX. The incoming magnetic energy, $W_{\mathrm{in}} = \int_{\mathcal{V}} \mathrm{d}^3 x \nabla \cdot \mathbf{S}_{\mathrm{in}}$, is about 1.4 MW. Here $\mathbf{S}_{\mathrm{in}} = (E_Y B_Z)/\mu_0 \mathbf{e}_R$ is the incoming Poynting flux associated with the reconnecting magnetic component B_Z and the reconnection electric field E_Y, where $\mathbf{e}_R$ is the unit vector along the radial (inflow) direction. Similar to the previous symmetric case, more than 50% of the incoming

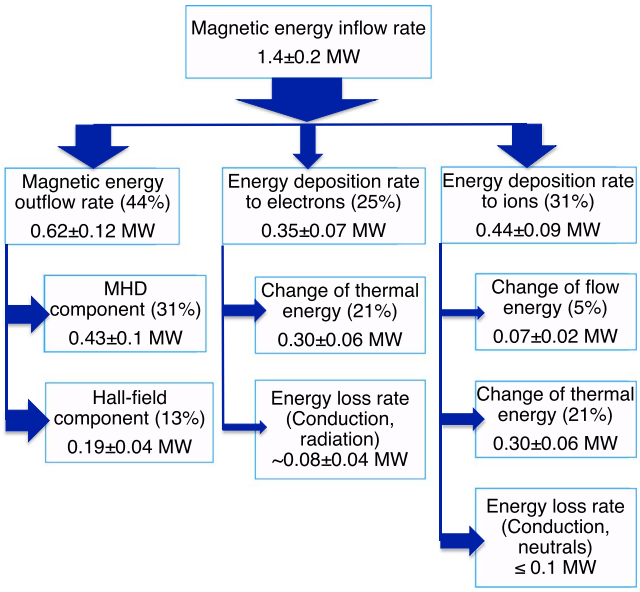

Figure 10. Energy inventory during asymmetric reconnection in the ion diffusion region in MRX. More than 50% of the incoming magnetic energy is converted to electrons and ions. The electron energy gain is comparable to the ion energy gain, which is different from the symmetric case where ions gain about twice more energy than electrons. The energy gain of both electrons and ions are dominated by the thermal component.

magnetic energy is converted to ions and electrons. Energy deposition rates to electrons and ions are computed by the volume integral of $\mathbf{J}_e \cdot \mathbf{E}$ and $\mathbf{J}_i \cdot \mathbf{E}$ respectively. Both electron and ion energy gains are dominated by thermal energy increase, which is also similar to the symmetric case. It is worth to note that the ion flow energy increase is only 5% of the total incoming magnetic energy, which means that the average ion outflow is much less than the hybrid Alfvén velocity V_{Ah}; the ion flow energy increase will be 50% of the incoming magnetic energy, if the average ion outflow speed reaches V_{Ah}. This result disagrees with the theoretical expectation by *Cassak and Shay* [2007]. This relatively small ion outflow speed is due to the lack of the large in-plane electric field, which inhibits the development of the ion outflow especially near the high-density-side separatrices, as shown in Figure 2b.

The energy inventory during asymmetric, antiparallel reconnection shows that the energy gain of electrons is comparable to that of ions, which is different from the symmetric case. The increase of the electron energy gain is due to the additional energy gain near the low-density side separatrices. As demonstrated in Figure 8 and explained in section 5, there is a significant amount of the electron energy gain near the low-density side separatrices associated with the parallel electric field as well as the diamagnetic current. On the other hand, the ion energy gain decreases due to both the small in-plain electric field near the high-density-side separatrices and the ion flow pattern near the low-density side separatrices. For the previous symmetric case, the value of $\mathbf{J}_i \cdot \mathbf{E}$, which is the ion energy gain per unit time and unit volume, ranges from 30 to 40 W/cm^3 near the separatrices. For asymmetric case, as shown in Figure 11, the value of $\mathbf{J}_i \cdot \mathbf{E}$ becomes about 15 W/cm^3. This decrease is directly related to the small in-plane electric field (~150 V/m), which is much smaller than a typical value of ~600 V/m for the symmetric case. The ion energy gain near the low-density side separatrices is noticeably negligible, although the in-plane electric field is large (~600 V/m). This is because the majority of ions from the high-density side do not across the low-density side separatrices due to the electrostatic potential barrier. As a result, the ion flow direction there is mostly parallel to the field lines as shown in Figure 2b and most ions do not gain energy from the large in-plane electric field. It is also

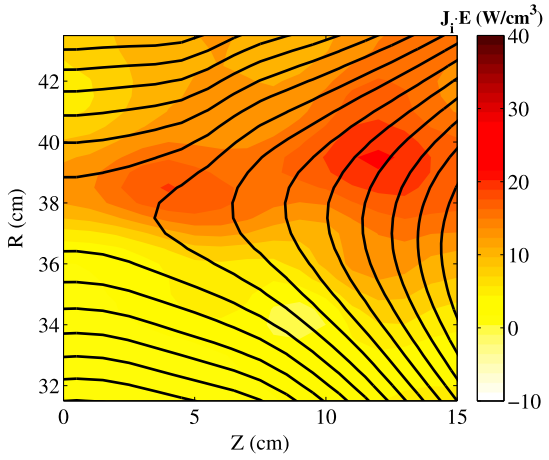

Figure 11. Profile of ion energy gain from the electric field, $\mathbf{J}_i \cdot \mathbf{E}$. Despite the large in-plane electric field near the low-density side separatrices, most ions from the high-density side do not obtain significant energy since they remain in the exhaust region.

worth noting that the ratio of the ion to electron energy gain is completely different for each side; on the low-density side, the electron energy gain is dominant over the ion energy gain, while it is the ions that dominate the energy gain on the high-density side.

This energy inventory for asymmetric reconnection in MRX indicates that magnetic reconnection still effectively converts magnetic energy to plasma energy, but detailed processes of energy conversion are different from the symmetric case. Changes in the mean field profiles, especially in the Hall fields, impact on details of the energy inventory. In particular, the ion and electron energy gain become comparable. Moreover, the outgoing component of the Poynting flux is dominated by the MHD component $\left(\mathbf{S}_{\mathrm{MHD}} = -\left(E_Y B_R/\mu_0\right)\mathbf{e}_Z\right)$ rather than the component associated with the Hall fields $\left(\mathbf{S}_{\mathrm{Hall}} = \left(E_R B_Y/\mu_0\right)\mathbf{e}_Z - \left(E_Z B_Y/\mu_0\right)\mathbf{e}_R\right)$, since the out-of-plane Hall magnetic field and the in-plane electric field become small on the low-density side and on the high-density side, respectively.

7. Summary

In MRX, typical features of asymmetric reconnection such as large density gradients near the low-density side separatrices, asymmetric in-plane electric field, and bipolar out-of-plane Hall magnetic field are observed. These features are consistent with space observations and numerical simulations. The changes of the Hall fields (out-of-plane magnetic field and in-plane electrostatic field) can be explained by the electron force balance, which is affected by the density asymmetry. The large density gradients near the low-density side separatrices are due to the large in-plane electrostatic potential, which prevents most ions from crossing the low-density side separatrices.

Detailed analysis of electron heating near the low-density side separatrices reveals that the parallel electric field is most likely responsible for the observed heating. Although large fluctuations by LHDI are observed where large density gradients exist, there is no strong correlation between the fluctuation amplitude and the electron temperature in the exhaust region. The comparison between 3-D and 2-D simulations also shows that LHDI-driven fluctuations do not play a major role in electron energization but the fluctuations may contribute to electron thermalization.

The amount of the bulk electron heating is proportional to the incoming magnetic energy per an electron-ion pair but is larger than space observations reported in *Phan et al.* [2013]. This discrepancy may be explained by differences of the boundary condition as well as of the measurement location. Due to the limited system size in MRX, the electron temperature measurement is conducted only about $2d_i$ away from the X line. The analysis of seven Cluster events supports the assertion that the average electron temperature in the exhaust region is relatively larger near the X line. Moreover, the detailed processes of electron heating in MRX may be different from those in space, due to the existence of collisions and the strong density pileup in the exhaust region.

The $\mathbf{J}_e \cdot \mathbf{E}$ profile raises an interesting question regarding the role of the diamagnetic current. Due to the large density gradients near the low-density side separatrices, the contribution from $\mathbf{J}_{eD} \cdot \mathbf{E}$ is dominant there. However, in terms of electron heating, that contribution is irrelevant, because there is no corresponding single-particle drift. The energy gain associated with the diamagnetic current is the same as the required energy to overcome the large pressure gradient and contributes increase of the electron enthalpy.

Finally, a quantitative study of the energy inventory during asymmetric reconnection is conducted in the ion diffusion region in MRX. Similar to the symmetric case, about 50% of the incoming magnetic energy is converted to plasma energy. Details of the energy inventory are, on the other hand, different. In particular, the electron energy gain becomes comparable to the ion energy gain. Between the two outgoing components of the Poynting flux, the MHD component becomes larger than the Hall field component. Since this energy inventory is conducted in MRX plasmas with a relatively small system size, it is interesting to see whether space observations show similar results or not. Utilizing MMS (Magnetospheric Multiscale) data from events at the dayside magnetopause and employing similar approach described in *Eastwood et al.* [2013b], the cross comparison may be achieved.

Although the current study extends our knowledge on plasma energization during reconnection, it does not cover reconnection with a guide field. Reconnection with a guide field shows different profiles of the Hall fields [*Tharp et al.*, 2012] as well as the density profile [*Fox et al.*, 2017], which means that processes of plasma energization are different during reconnection with a significant guide field. Plasma energization during guide field reconnection is a potential future research topic.

Acknowledgments
This work is supported by the DOE contract DE-AC0209CH11466, and NASA grant NNH14AX63I. The authors thank R. Cutler for technical support. Data used for this manuscript are available in the DataSpace of Princeton University (http://arks.princeton.edu/ark:/88435/dsp01x920g025r).

References

Argall, M. R. (2014), Estimating proximity to the asymmetric reconnection X-line, PhD thesis, Univ. of New Hampshire, Durham.
Aunai, N., G. Belmont, and R. Smets (2011), Energy budgets in collisionless magnetic reconnection: Ion heating and bulk acceleration, *Phys. Plasmas*, *18*(12), 122901.
Bowers, K. J., B. J. Albright, L. Yin, B. Bergen, and T. J. T. Kwan (2008), Ultrahigh performance three-dimensional electromagnetic relativistic kinetic plasma simulation, *Phys. Plasmas*, *15*(5), 55703.
Braginskii, S. I. (1965), Transport processes in a plasma, in *Reviews of Plasma Physics*, vol. 1, edited by M. A. Leontovich, pp. 205–311, Consultants Bureau, New York.
Carter, T. A., H. Ji, F. Trintchouk, M. Yamada, and R. M. Kulsrud (2001), Measurement of lower-hybrid drift turbulence in a reconnecting current sheet, *Phys. Rev. Lett.*, *88*, 15001.
Cassak, P. A., and M. A. Shay (2007), Scaling of asymmetric magnetic reconnection: General theory and collisional simulations, *Phys. Plasmas*, *14*(10), 102114.
Chen, S.-L., and T. Sekiguchi (1965), Instantaneous direct-display system of plasma parameters by means of triple probe, *J. Appl. Phys.*, *36*(8), 2363–2375.
Dahlin, J. T., J. F. Drake, and M. Swisdak (2014), The mechanisms of electron heating and acceleration during magnetic reconnection, *Phys. Plasmas*, *21*(9), 92304, doi:10.1063/1.4894484.
Daughton, W. (2003), Electromagnetic properties of the lower-hybrid drift instability in a thin current sheet, *Phys. Plasmas*, *10*(8), 3103–3119, doi:10.1063/1.1594724.
Eastwood, J. P., T. D. Phan, M. ÃŸieroset, M. A. Shay, K. Malakit, M. Swisdak, J. F. Drake, and A. Masters (2013a), Influence of asymmetries and guide fields on the magnetic reconnection diffusion region in collisionless space plasmas, *Plasma Phys. Controlled Fusion*, *55*(12), 124001.
Eastwood, J. P., T. D. Phan, J. F. Drake, M. A. Shay, A. L. Borg, B. Lavraud, and M. G. G. T. Taylor (2013b), Energy partition in magnetic reconnection in Earth's magnetotail, *Phys. Rev. Lett.*, *110*, 225001.
Egedal, J., A. Le, P. L. Pritchett, and W. Daughton (2011), Electron dynamics in two-dimensional asymmetric anti-parallel reconnection, *Phys. Plasmas*, *18*(10), 102901.
Fiksel, G., D. J. D. Hartog, and P. W. Fontana (1998), An optical probe for local measurements of fast plasma ion dynamics, *Rev. Sci. Instrum.*, *69*(5), 2024–2026.
Fox, W., F. Sciortino, A. v. Stechow, J. Jara-Almonte, J. Yoo, H. Ji, and M. Yamada (2017), Experimental verification of the role of electron pressure in fast magnetic reconnection with a guide field, *Phys. Rev. Lett.*, *118*, 125002, doi:10.1103/PhysRevLett.118.125002.
Goldston, R. J., and P. H. Rutherford (2000), *Introduction to Plasma Physics*, Taylor and Francis Group, LLC, New York.
Graham, D. B., Y. V. Khotyaintsev, A. Vaivads, M. André, and A. N. Fazakerley (2014), Electron dynamics in the diffusion region of an asymmetric magnetic reconnection, *Phys. Rev. Lett.*, *112*, 215004, doi:10.1103/PhysRevLett.112.215004.
Haggerty, C. C., M. A. Shay, J. F. Drake, T. D. Phan, and C. T. McHugh (2015), The competition of electron and ion heating during magnetic reconnection, *Geophys. Res. Lett.*, *42*, 9657–9665, doi:10.1002/2015GL065961.
Jara-Almonte, J., W. Daughton, and H. Ji (2014), Debye scale turbulence within the electron diffusion layer during magnetic reconnection, *Phys. Plasmas*, *21*(3), 32114, doi:10.1063/1.4867868.
Ji, H., and W. Daughton (2011), Phase diagram for magnetic reconnection in heliophysical, astrophysical, and laboratory plasmas, *Phys. Plasmas*, *18*(11), 111207.
Ji, H., S. Terry, M. Yamada, R. Kulsrud, A. Kuritsyn, and Y. Ren (2004), Electromagnetic fluctuations during fast reconnection in a laboratory plasma, *Phys. Rev. Lett.*, *92*, 115001.
Khotyaintsev, Y. V., A. Vaivads, A. Retinò, M. André, C. J. Owen, and H. Nilsson (2006), Formation of inner structure of a reconnection separatrix region, *Phys. Rev. Lett.*, *97*, 205003.
Krucker, S., H. S. Hudson, L. Glesener, S. M. White, S. Masuda, J.-P. Wuelser, and R. P. Lin (2010), Measurements of the coronal acceleration region of a solar flare, *Astrophys. J.*, *714*(2), 1108.
Le, A., J. Egedal, W. Daughton, V. Roytershteyn, H. Karimabadi, and C. Forest (2015), Transition in electron physics of magnetic reconnection in weakly collisional plasma, *J. Plasma Phys.*, *81*, 305810108.
Le, A., J. Egedal, and W. Daughton (2016), Two-stage bulk electron heating in the diffusion region of anti-parallel symmetric reconnection, *Phys. Plasmas*, *23*(10), 102109, doi:10.1063/1.4964768.
Lin, R., and H. Hudson (1976), Non-thermal processes in large solar flares, *Sol. Phys.*, *50*, 153–178.
Lin, R. P., et al. (2003), Rhessi observations of particle acceleration and energy release in an intense solar gamma-ray line flare, *Astrophys. J. Lett.*, *595*(2), L69–L76.
Malakit, K., M. A. Shay, P. A. Cassak, and C. Bard (2010), Scaling of asymmetric magnetic reconnection: Kinetic particle-in-cell simulations, *J. Geophys. Res.*, *115*, A10223, doi:10.1029/2010JA015452.
Mozer, F. S., and P. L. Pritchett (2011), Electron physics of asymmetric magnetic field reconnection, *Space Sci. Rev.*, *158*(1), 119–143.
Mozer, F. S., V. Angelopoulos, J. Bonnell, K. H. Glassmeier, and J. P. McFadden (2008a), THEMIS observations of modified Hall fields in asymmetric magnetic field reconnection, *Geophys. Res. Lett.*, *35*, L17S04, doi:10.1029/2007GL033033.
Mozer, F. S., P. L. Pritchett, J. Bonnell, D. Sundkvist, and M. T. Chang (2008b), Observations and simulations of asymmetric magnetic field reconnection, *J. Geophys. Res.*, *113*, A00C03, doi:10.1029/2008JA013535.
Mozer, F. S., M. Wilber, and J. F. Drake (2011), Wave associated anomalous drag during magnetic field reconnection, *Phys. Plasmas*, *18*(10), 102902.
Na, B., J. Yoo, J. Jara-Almonte, H. Ji, W. Fox, and M. Yamada (2017), A double-sided electron energy analyzer for measurements of non-Maxwellian electron energy distribution, to be published.
Phan, T. D., M. A. Shay, J. T. Gosling, M. Fujimoto, J. F. Drake, G. Paschmann, M. Oieroset, J. P. Eastwood, and V. Angelopoulos (2013), Electron bulk heating in magnetic reconnection at Earth's magnetopause: Dependence on the inflow Alfvén speed and magnetic shear, *Geophys. Res. Lett.*, *40*(17), 4475–4480, doi:10.1002/grl.50917.
Pritchett, P. L. (2008), Energetic electron acceleration during multi-island coalescence, *Phys. Plasmas*, *15*(10), 102105.
Pritchett, P. L., F. S. Mozer, and M. Wilber (2012), Intense perpendicular electric fields associated with three-dimensional magnetic reconnection at the subsolar magnetopause, *J. Geophys. Res.*, *117*, A06212, doi:10.1029/2012JA017533.
Retinò, A., et al. (2005), Cluster multispacecraft observations at the high-latitude dusk side magnetopause: Implications for continuous and component magnetic reconnection, *Ann. Geophys.*, *23*(2), 461–473, doi:10.5194/angeo-23-461-2005.
Roytershteyn, V., W. Daughton, H. Karimabadi, and F. S. Mozer (2012), Influence of the lower-hybrid drift instability on magnetic reconnection in asymmetric configurations, *Phys. Rev. Lett.*, *108*, 185001.
Roytershteyn, V., S. Dorfman, W. Daughton, H. Ji, M. Yamada, and H. Karimabadi (2013), Electromagnetic instability of thin reconnection layers: Comparison of three-dimensional simulations with MRX observations, *Phys. Plasmas*, *20*(6), 61212.

Shay, M. A., C. C. Haggerty, T. D. Phan, J. F. Drake, P. A. Cassak, P. Wu, M. Oieroset, M. Swisdak, and K. Malakit (2014), Electron heating during magnetic reconnection: A simulation scaling study, *Phys. Plasmas*, *21*(12), 122902.

Tanaka, K. G., et al. (2008), Effects on magnetic reconnection of a density asymmetry across the current sheet, *Ann. Geophys.*, *26*(8), 2471–2483, doi:10.5194/angeo-26-2471-2008.

Tang, X., C. Cattell, J. Dombeck, L. Dai, L. B. Wilson, A. Breneman, and A. Hupach (2013), THEMIS observations of the magnetopause electron diffusion region: Large amplitude waves and heated electrons, *Geophys. Res. Lett.*, *40*, 2884–2890, doi:10.1002/grl.50565.

Tharp, T. D., M. Yamada, H. Ji, E. Lawrence, S. Dorfman, C. E. Myers, and J. Yoo (2012), Quantitative study of guide-field effects on hall reconnection in a laboratory plasma, *Phys. Rev. Lett.*, *109*, 165002.

Vaivads, A., Y. Khotyaintsev, M. André, A. Retinò, S. C. Buchert, B. N. Rogers, P. Décréau, G. Paschmann, and T. D. Phan (2004), Structure of the magnetic reconnection diffusion region from four-spacecraft observations, *Phys. Rev. Lett.*, *93*, 105001.

Yamada, M., H. Ji, S. Hsu, T. Carter, R. Kulsrud, N. Bretz, F. Jobes, Y. Ono, and F. Perkins (1997), Study of driven magnetic reconnection in a laboratory plasma, *Phys. Plasmas*, *4*(5), 1936–1944.

Yamada, M., J. Yoo, J. Jara-Almonte, H. Ji, R. M. Kulsrud, and C. E. Myers (2014), Conversion of magnetic energy in the magnetic reconnection layer of a laboratory plasma, *Nat. Commun.*, *5*, 4474.

Yamada, M., J. Yoo, J. Jara-Almonte, W. Daughton, H. Ji, R. M. Kulsrud, and C. E. Myers (2015), Study of energy conversion and partitioning in the magnetic reconnection layer of a laboratory plasma, *Phys. Plasmas*, *22*(5), 56501, doi:10.1063/1.4920960.

Yoo, J., M. Yamada, H. Ji, and C. E. Myers (2013), Observation of ion acceleration and heating during collisionless magnetic reconnection in a laboratory plasma, *Phys. Rev. Lett.*, *110*, 215007.

Yoo, J., M. Yamada, H. Ji, J. Jara-Almonte, C. E. Myers, and L.-J. Chen (2014a), Laboratory study of magnetic reconnection with a density asymmetry across the current sheet, *Phys. Rev. Lett.*, *113*, 95002.

Yoo, J., M. Yamada, H. Ji, J. Jara-Almonte, and C. E. Myers (2014b), Bulk ion acceleration and particle heating during magnetic reconnection in a laboratory plasma, *Phys. Plasmas*, *21*(5), 55706.